Advanced Composites and Hybrid Materials (2023) 6:143
https://doi.org/10.1007/s42114-023-00715-3

RESEARCH

Rigid-flexible double coating silicon oxide composed of pitch pyrolytic carbon and polyvinyl alcohol/polyethyleneimine/carbon nanotubes as high-performance anode material for lithium-ion battery

Chunping Hou[1,2,3] · Haidong Xie[1] · Yuqing Qu[1] · Hui Tian[1] · Jingying Jiang[1] · Hui Lu[1,3] · Shaolin Yang[1,3] · Yong Ma[4]

Received: 14 May 2023 / Revised: 20 June 2023 / Accepted: 21 June 2023 / Published online: 25 July 2023

Abstract
Silicon oxide (SiO_x) is considered to be one of the most promising anodes of lithium-ion batteries for its advantageous capacity and abundant natural resources. However, the practical application of SiO_x is facing great challenges due to its low conductivity and poor cycle performance. In order to accelerate the commercial application of SiO_x, we constructed a pitch pyrolytic carbon rigid coating and a highly conductive polyvinyl alcohol/polyethyleneimine/carbon nanotubes (PVA/PEI/CNTs) flexible coating on the surface of micron-sized SiO_x. The synergistic effect of the double coating enhances the conductivity of SiO_x, reduces the strain stress caused by the volume change of SiO_x, prevents the particles from breaking away from the current collector, and maintains the structural integrity of SiO_x under long-term cycling. The obtained SiO_x/E@CPPC anode exhibits high initial coulombic efficiency (73.91%), excellent cycle stability (645.8 mAh·g^{-1} after 700 cycles at 0.5 A·g^{-1}) and excellent rate performance (407.1 mAh·g^{-1} at 5 A·g^{-1}). The double coating makes SiO_x/E@CPPC composites have a good application prospect in lithium-ion batteries.

Keywords SiO_x · Rigid-flexible coating · Anode materials · Electrochemcial performances

1 Introduction

As a convenient, efficient, and environmentally friendly energy storage device, lithium-ion batteries have been widely used in the electric vehicles industry [1–4]. In order to compete with fuel vehicles, electric vehicles need to provide about 800 km of mileage on a single charge. Although the mileage of electric vehicles can be extended by loading more batteries, the corresponding increase in weight and cost will be unacceptable [5]. Therefore, batteries with higher energy density are a better choice. The specific capacity of the mainstream anode material with graphite is only 372 mAh·g^{-1} [6], which cannot meet the requirements of high energy density of lithium-ion batteries. Si can output ultra-high specific capacity (3580 mAh·g^{-1}) at a suitable working potential [7]. Unfortunately, the drastic volume fluctuation (~300%) of Si during the cycle and the formation of unstable solid electrolyte interface (SEI) will lead to the instability of the electrode material [8]. Therefore, people have turned their attention to silicon oxide (SiO_x), a derivative material of Si with high specific capacity, but lower cost and smaller volume change.

SiO_x forms Li_2O and Li silicate during lithiation, and it is helpful to establish a stable SEI layer and adapt to the volume change of SiO_x [9]. However, the problems of low initial coulombic efficiency, low conductivity, and high volume fluctuation (~200%) of SiO_x still cannot be ignored [10]. In this regard, researchers have made many efforts, including surface coating [11], element doping [12], compounding with high conductive materials [13], and designing special structures [14]. It is more common to construct a coating

✉ Chunping Hou
houcp@nmu.edu.cn

✉ Yong Ma
mayong@sdust.edu.cn

1 College of Materials Science and Engineering, North Minzu University, Yinchuan 750021, People's Republic of China

2 Bolt New Material (Yinchuan) Co, Ltd, Yinchuan 750002, People's Republic of China

3 Ningxia Research Center of Silicon Target and Silicon-Carbon Negative Material Engineering Technology, Yinchuan 750021, People's Republic of China

4 School of Materials Science and Engineering, Shandong University of Science and Technology, Qindao 266590, People's Republic of China

layer on the surface of SiO_x, which is usually mainly coated with carbon materials. However, these coatings are mostly rigid coatings, which are difficult to maintain the structural integrity of SiO_x particles during long-term charging and discharging.

In recent years, the method of adding a polymer flexible coating to SiO_x has attracted the attention of researchers. Flexible coating can reduce the strain stress caused by volume changes and prevent particles from breaking away from the current collector. For example, Park et al. [15] used poly(3,4-ethylenedioxythiophene):polystyrene sulfonic acid (PEDOT:PSS) with certain mechanical flexibility and high conductivity as a flexible coating and as a conductive path in the electrode. It also makes SiO_x not undergo large volume changes during the cycle. Li et al. [16] prepared a flexible coating layer of lithium polyacrylate/carbon nanotubes (Li-PAA/CNTs). The uniform Li conductive layer and the flexible Li-PAA interface provide a fast electronic path for SiO_x/C particles and maintain the structural integrity of micron-sized C-SiO_x/C particles. Kang et al. [17] used PVDF with appropriate Young's modulus as a soft and deformable elastomer buffer matrix, and the prepared 3D SiO_x-based flexible self-supporting membrane anode showed extremely high specific capacity and cycle stability. However, the conductivity of traditional flexible coatings is generally lower than that of rigid coatings, and rigid coatings are difficult to maintain the structural stability of SiO_x in long-term cycles.

Here, we firstly compounded SiO_x with ECP-600JD having excellent conductivity to improve the conductivity of the material, and then used pitch to prepare a rigid carbon coating. Secondly, a flexible interface polyvinyl alcohol/polyethyleneimine/carbon nanotubes (PVA/PEI/CNTs) with high conductivity was constructed on the surface of SiO_x/E@C particles by using PVA with high tensile strength and excellent flexibility [18], PEI and CNTs. Accordingly, SiO_x/E@CPPC composites with rigid-flexible double coating were prepared. The double coating makes SiO_x/E@CPPC have better cycle stability, high initial efficiency, and fast lithium insertion/extraction kinetics.

2 Experimental section

2.1 Materials

SiO_x and pitch was provided by Bolt New Materials (Yinchuan) Co., Ltd. Ketjen Black (EP-600JD) was produced by Japan Lion King Co., Ltd. Polyvinyl alcohol (PVA) was purchased from Shanghai MackLin Biochemical Technology Co., Ltd. Polyethyleneimine (PEI, 50 wt.% aqueous solution) was purchased from Shanghai Aladdin Biochemical Technology Co., Ltd. Hydroxylated multi-walled carbon nanotubes (CNTs) were bought from Nanjing Xianfeng Nanomaterials Technology Co., Ltd.

2.2 Fabrication of SiO_x/ECP-600JD(SiO_x/ECP)

SiO_x/ECP-600D (SiO_x/ECP) composites were obtained by adding 2 g SiO_x and 0.1 g ECP-600 JD into the ball milling tank, then adding 84 g ZrO_2 balls with a diameter of 1 mm, and ball milling for 1 h at 420 rpm in a planetary ball mill.

2.3 Fabrication of SiO_x/ECP@Carbon (SiO_x/E@C)

2.1 g SiO_x/ECP and 0.45 g pitch were added to the ball mill, and 102 g ZrO_2 balls with a diameter of 1 mm were added. The precursor was obtained by ball milling at 420 rpm for 1 h in a planetary ball mill. Finally, SiO_x/ECP@Carbon (SiO_x/E@C) composites were obtained by heating to 300 °C at 5 °C·min^{-1} for 2 h in argon atmosphere, and then heating to 900 °C at 5 °C·min^{-1} for 2 h.

2.4 Fabrication of SiO_x/ECP@Carbon/PVA/PEI/CNTs (SiO_x/E@CPPC)

5.0 g PVA was added to 95.0 g deionized water and stirred at 90 °C for 2 h to completely dissolve PVA into 5 wt.% PVA aqueous solution (solution A). The 2.0 g PEI solution was added to 8.0 g deionized water, stirred evenly, and diluted into 10 wt.% PEI aqueous solution (solution B). After 0.5 g solution A, 0.1 g solution B, and 0.5 g SiO_x/E@C, 50 mL deionized water was added, stirred for 1 h, and the mixed solution C was obtained after ultrasonication for 1 h. 0.01 g CNTs were added into 50 mL deionized water, stirring for 2 h, and ultrasonic for 2 h to obtain a well-dispersed CNTs solution D. The solution C was added into solution D dropwise. After standing for 24 h, the mixed solution was centrifuged at 10,000 rpm for 0.5 h and then vacuum dried at 50 °C for 10 h to obtain SiO_x/ECP@Carbon/PVA/PEI/CNTs (SiO_x/E@CPPC) composites.

2.5 Characterization

The phase composition of the composites was analyzed by XRD-6000 diffractometer using Cu Kα radiation to collect XRD patterns. The infrared spectrum was tested using a WQF-520A Fourier transform infrared spectrometer with a test range of 4000–400 cm^{-1}. Scanning electron microscopy (SEM) was performed on SIGMA 500 to study the morphology of the material. Transmission electron microscopy analysis was performed using a JEM-2100 instrument. Thermogravimetric (TG) analysis was performed on the STA449F3 instrument. The sample was heated to 800 °C in air at 15 °C·min^{-1} and then held for 30 min. The specific surface area and the pore size distribution were analyzed on

3H-2000PM1 instrument. The surface chemical characteristics of the doped elements were observed by ESCALAB Xi + X-ray photoelectron spectrometer.

2.6 Electrochemical characterization

The working electrodes were fabricated by casting slurry containing active material, conductive additive (Super P) and binder (polyacrylic acid, MW = 100,000) with a weight ratio of 70:10:20 on copper-foil current collector, followed by drying in a vacuum oven at 80 °C for 10 h. The electrochemical properties of the as-prepared samples were carried out using 2025 coin-type cells assembled in an argon-filled glovebox (< 0.2 ppm of oxygen and water). Lithium metal was applied as the counter electrode, the microporous membrane (Celgard 2400) as separator, and 1 M LiPF6 in a mixture of EC, EMC, and DMC (volume ratio of 1:1:1) + 6 vol.% FEC additive adopted as electrolyte. Galvanostatic charge–discharge profiles, cycle life, rate capability, and galvanostatic intermittent titration technique (GITT) tests were performed using a LAND CT2001A battery test system within the voltage range of 0.01–2.0 V (vs. Li/Li^+). Cyclic voltammetry (CV) at various sweep rates of 0.1–1.0 $mV{\cdot}s^{-1}$ and electrochemical impedance spectroscopy (EIS) analysis with a voltage amplitude of 5 mV in the frequency range from 100 kHz to 0.01 Hz were both conducted on Chi660e electrochemical workstation.

3 Results and discussion

3.1 Morphology and characterization of SiO_x/E@CPPC

Figure 1 shows the design and construction process of micron-sized SiO_x/E@CPPC particles. Firstly, SiO_x and ECP-600JD are mixed by ball milling. ECP-600JD is a Ketjen Black material with high conductivity, which can improve the conductivity of the composite material. Secondly, a rigid carbon coating formed by pyrolysis of pitch is coated on the surface of SiO_x/ECP by ball milling and high temperature calcination. Finally, SiO_x/E@C is combined with PVA, PEI, and CNTs to form a conductive flexible coating layer. PEI is a cationic polymer electrolyte that can make the particle surface positively charged. The Zeta potential of SiO_x/E@C in water is − 32.6 mV. After PEI modification, the surface of SiO_x/E@CPP is positively charged (+ 21.8 mV), while the surface of CNTs is negatively charged (− 19.4 mV). Therefore, after mixing SiO_x/E@CPP with CNTs solution, CNTs will be firmly fixed on the

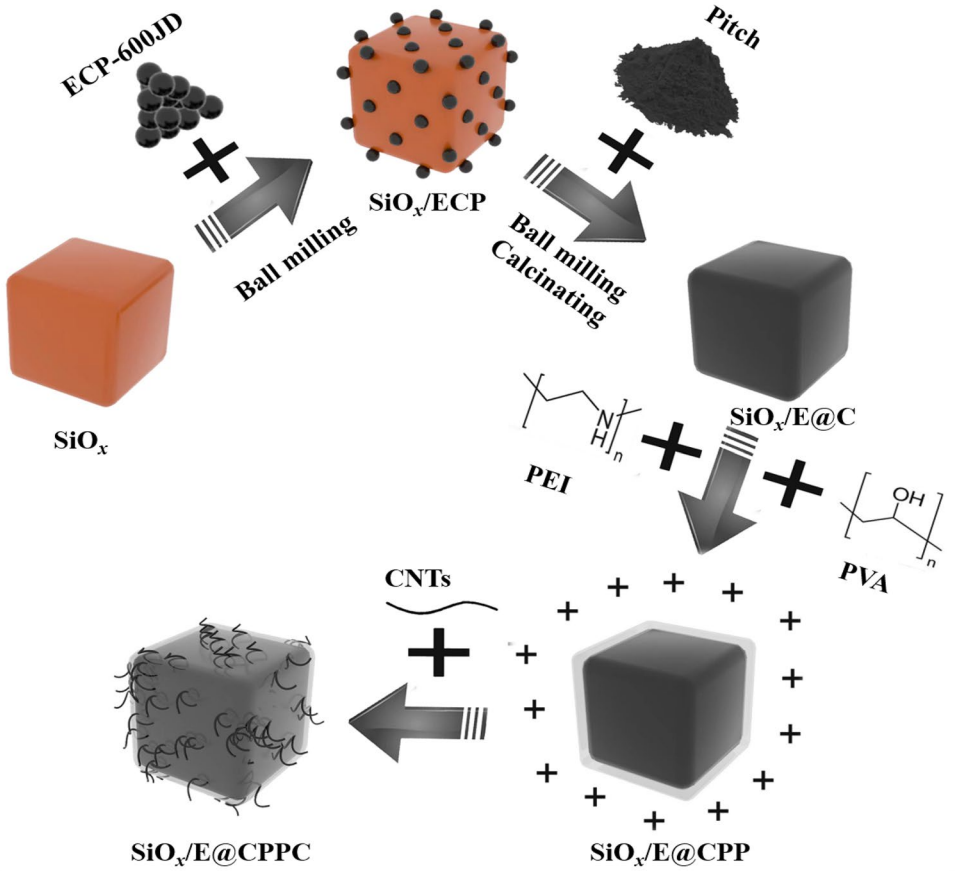

Fig. 1 Schematic chart of the fabrication for SiO_x/E@CPPC

surface of SiO_x/E@CPP under the action of electrostatic adsorption to construct a good conductive network. At the same time, the abundant hydroxyl groups in PVA can be better combined with the abundant carboxyl groups in the binder PAA to maintain the integrity of the SiO_x/E@CPPC electrode during the cycling process.

The XRD patterns of SiO_x, ECP-600JD, SiO_x/ECP, SiO_x/E@C, and SiO_x/E@CPPC are shown in Fig. 2a. There are two wide peaks of SiO_x at 2θ = 23° and 52°, indicating that the crystallinity of SiO_x is low, which is consistent with the relevant literature reports [19]. The wide dispersion peaks of ECP-600JD at 2θ = 23° and 44° correspond to the (002) and (101) crystal planes of graphitized carbon, respectively [20, 21]. Due to the low content of ECP-600JD (the weight ratio of ECP-600JD to SiO_x is 1:20), no obvious characteristic diffraction peak of ECP-600JD is found in SiO_x/ECP. In the XRD pattern of SiO_x/E@C, the amorphous carbon layer formed by pitch pyrolysis overlaps with the broad peak of 23° in SiO_x [22], and the diffraction peaks at 2θ = 28.4°, 47.3°, and 56.1° belong to the (111), (220), and (311) crystal planes of cubic Si (JCPDS No.27–1402), respectively. This is due to the disproportionation reaction at 900 °C of some SiO_x [23]. The diffraction peaks of SiO_x/E@CPPC are similar to those of SiO_x/E@C, but the diffraction peaks of Si in SiO_x/E@CPPC is weaker than those of SiO_x/E@C, indicating that SiO_x/E@CPPC are coated with PVA and PEI [16].

Figure 2b exhibits the FT-IR spectra of SiO_x, ECP-600JD, SiO_x/ECP, SiO_x/E@C, SiO_x/E@CPPC, PEI, PVA, and CNTs. The characteristic peaks of SiO_x are broad peaks at 465 cm^{-1}, 790 cm^{-1}, and 1100 cm^{-1}, which represent Si-O bending vibration, Si-O-Si symmetric stretching vibration, and Si-O-Si antisymmetric stretching vibration, respectively [24]. At the same time, the peak at 1402 cm^{-1} represents C-H bending vibration [25], the peak at 1630 cm^{-1} represents O-H bending vibration [26], and the broad peaks at 3120 cm^{-1} and 3430 cm^{-1} represent O-H stretching vibration [27, 28], which may be caused by the adsorption of H_2O in the air. The characteristic peaks of ECP-600JD are C-H bending vibration peaks at 1402 cm^{-1} and C=C stretching vibration peaks at 1624 cm^{-1} [29]. The diffraction peaks of SiO_x/ECP at about 1400 cm^{-1} and 1620 cm^{-1} are enhanced compared with the Si-O-Si peak at 1100 cm^{-1}, meaning that ECP-600JD is mixed with SiO_x. The diffraction peak intensity of SiO_x/E@C at about 1400 cm^{-1} and 1620 cm^{-1} are further enhanced, which is caused by the increase of C-H and C=C in the carbon coating generated by pitch pyrolysis. In the spectrum of PEI, the C-N stretching vibration peak [30], the C-N bending vibration peak [13], and the N-H bending vibration peak at 1274 cm^{-1}, 1450 cm^{-1}, and 1600 cm^{-1}, and the peaks at 2830 cm^{-1} and 2935 cm^{-1} is the C-H stretching peak [31, 32]. The C-O stretching vibration peak at 1043 cm^{-1} of PVA is viewed. Since PVA is rich in hydroxyl groups, it shows a very wide diffraction peak at

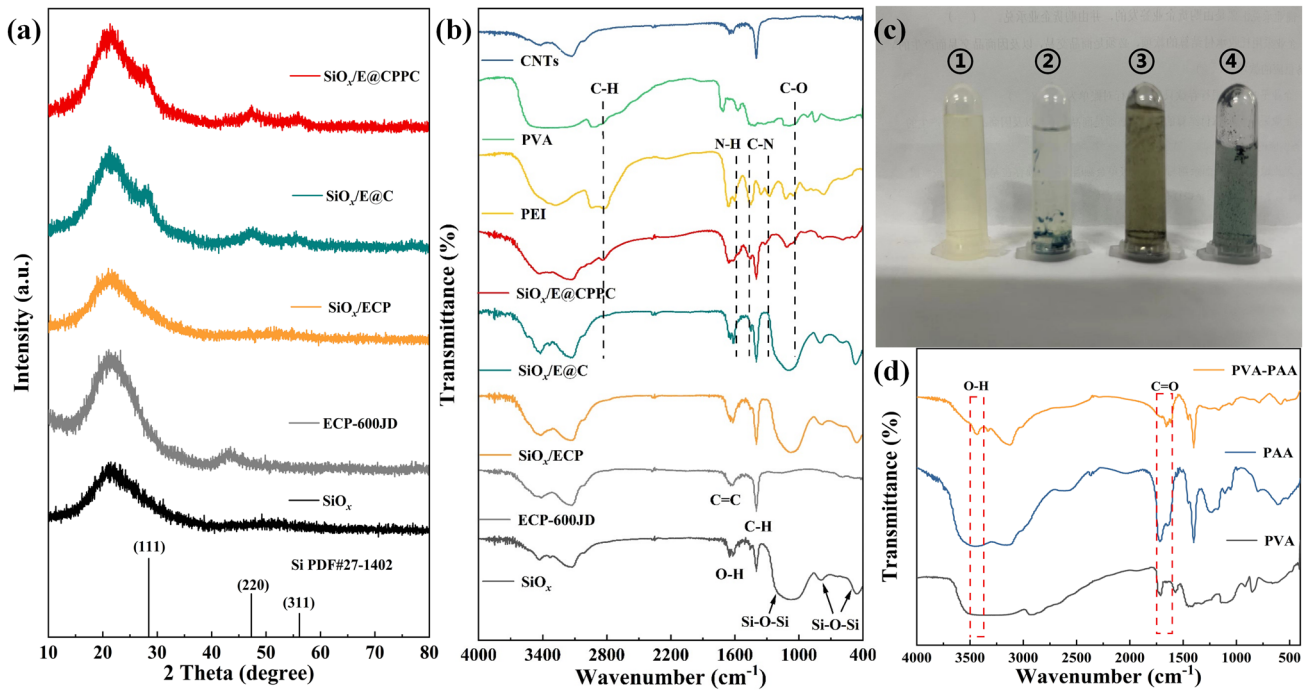

Fig. 2 **a** XRD patterns of SiO_x, ECP-600JD, SiO_x/ECP, SiO_x/E@C and SiO_x/E@CPPC; **b** FT-IR spectra of SiO_x, ECP-600JD, SiO_x/ECP, SiO_x/E@C, SiO_x/E@CPPC, PEI, PVA, and CNTs; **c** Optical images of I/KI solution, PVA in I/KI solution, SiO_x/E@C in I/KI solution, SiO_x/E@CPPC in I/KI solution; **d** FT-IR spectra of PVA, PAA, and PVA-PAA

3430 cm^{-1} [33–35]. The diffraction peaks of CNTs are similar to those of ECP-600JD. The diffraction peaks of C-H, N-H, C-N, and C-O can be found in SiO_x/E@CPPC, but not found in SiO_x/E@C. Meanwhile, the intensity of the three diffraction peaks (465 cm^{-1}, 790 cm^{-1}, and 1100 cm^{-1}) of Si-O decrease in comparison with SiO_x/E@C, implying that the surface of SiO_x/E@CPPC contains a large number of O-H, C-H, C=C, N-H, etc. This case demonstrates that SiO_x/E@C is coated with PVA, PEI, and CNTs.

The presence of PVA in the particles is further illustrated by the blue flocs produced by PVA in the mixed solution of I/KI. In Fig. 2c, ① is I/KI mixed solution, which is light yellow; ② is PVA in I/KI mixed solution, in which blue flocs appears and the color becomes lighter; ③ is SiO_x/E@C in I/KI mixed solution, in which the light-yellow solution appears black, the color becomes darker, and no blue floccules appear; ④ is the I/KI mixed solution, in which blue floccules appears, suggesting that PVA exists in SiO_x/E@CPPC. The spectra of PVA, PAA, and PVA-PAA shown in Fig. 2d confirm that PVA on the surface of the particles can interact with the binder PAA. After PVA and PAA are mixed and dried at 80 °C, the stretching vibration peak at 3430 cm^{-1} of O-H bond in PVA-PAA decreases and moves to low wavenumber. In addition, the stretching vibration peak (1720 cm^{-1}) of the C=O bond of PAA shifts to a lower wavenumber of 1700 cm^{-1}. The change illustrates that the esterification reaction occurs between PAA and PVA to form -COO- [36]. The strong interaction between PAA and PVA is beneficial to improve the integrity of the electrode, thereby reducing the structural damage of the electrode, helping to suppress the volume change of the silicon particles and maintain the integrity of the electrode, and ensuring good electrical contact between the active particles and the current collector.

As shown in the SEM image of Fig. S2, SiO_x is an irregular block object with a smooth surface and a particle size of 0.3 ~ 3 μm. Fig. S3 is the SEM image of ECP-600JD, in which ECP-600JD is spherical with a particle size of about 30 nm. ECP-600JD is a high-performance conductive carbon black with a specific surface area of about 1400 $m^2 \cdot g^{-1}$. It has a unique branched chain morphology and is easy to fully contact with the particles to form an efficient conductive network. Figure 3 displays the SEM images of SiO_x/ECP, SiO_x/E@C, and SiO_x/E@CPPC. It can be seen from SiO_x/ECP in Fig. 3a and d that ECP-600JD agglomerates on the surface of SiO_x particles. After coating with amorphous carbon generated by pyrolysis of asphalt, it can be seen from Fig. 3b and e that the surface of SiO_x/E@C becomes smooth and the particle size is basically unchanged. There are still some small particles (ECP-600JD) on the surface of SiO_x/E@C. Compared with the smooth surface of SiO_x/E@C, the particle surface of SiO_x/E@CPPC is rougher (Fig. 3c and f). The CNTs on the surface of SiO_x/E@CPPC are clearly visible, which realizes the coating of SiO_x/E@C particles. The length of CNTs is 0.5 ~ 2 μm, and CNTs have excellent chemical stability and excellent mechanical

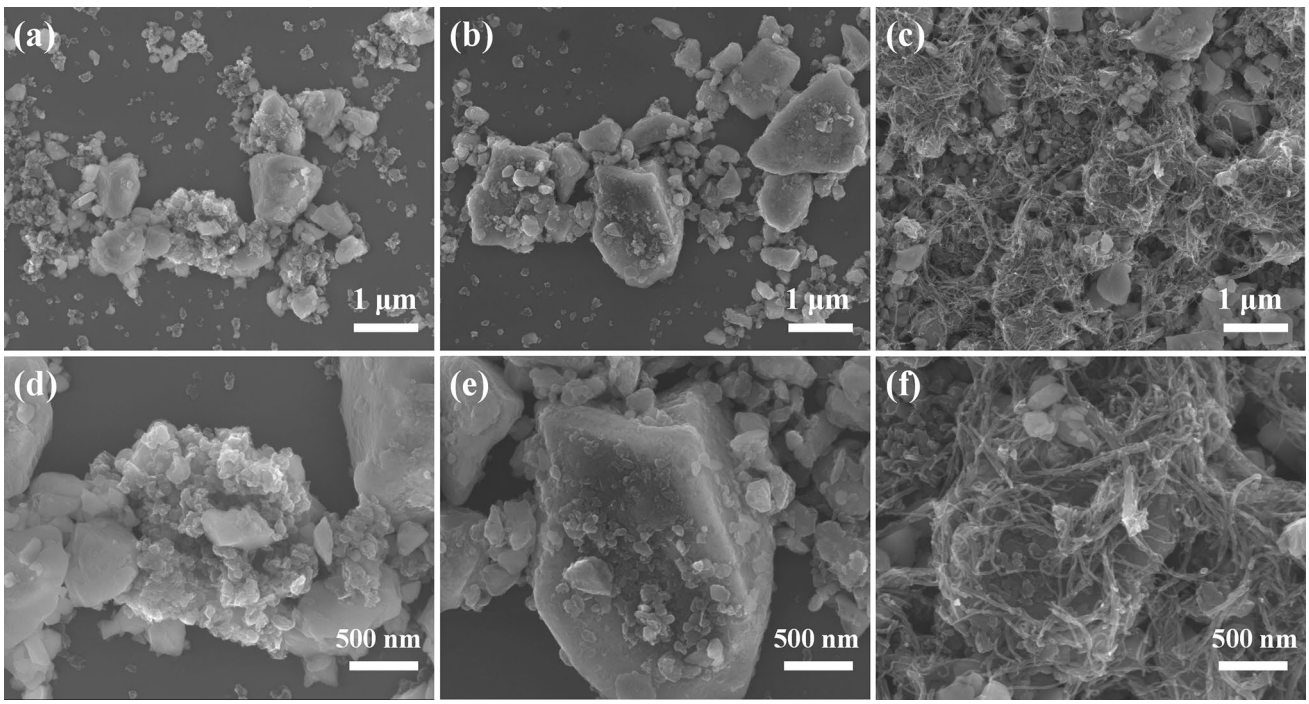

Fig. 3 **a**, **d** SEM images of SiO_x/ECP, **b**, **e** SiO_x/E@C, **c**, **f** SiO_x/E@CPPC

properties [37]. This structure not only ensures excellent electronic conductivity, but also significantly improves the mechanical properties of the composite interface, thus ensuring the good electrochemical performance and structural integrity of micron-sized SiO_x/E@CPPC particles.

Figure 4 exhibits the TEM images and EDS analysis results of SiO_x/E@CPPC. It can be seen from the 4a that SiO_x is coated with a carbon layer and CNTs presents on the surface of SiO_x/E@C particles. The EDS element distribution diagram of SiO_x/E@CPPC (Fig. 4b–e) confirm that C, O, Si, and N elements on the surface of the particles. C element is mainly distributed in the outermost layer, as well as N element and O element are mainly distributed in the middle layer, declaring that PVA/PEI/CNTs coating is formed on the surface of SiO_x/E@CPPC particles, and Si element is distributed in the innermost layer to form a core–shell structure.

For exploring the differences in the specific surface area and the pores of SiO_x/ECP, SiO_x/E@C, and SiO_x/E@CPPC, N_2 adsorption and desorption tests are performed (as shown in Fig. 5a and b). The isotherm of SiO_x/ECP is a typical type IV isotherm, and there is a large hysteresis loop in the high relative pressure region ($0.4 < P/P_0 < 0.8$), showing that it has a large number of mesopores [38, 39]. The specific surface area is 73.73 $m^2 \cdot g^{-1}$. The pore size of SiO_x/ECP is mainly distributed between 2 and 8 nm, and the total pore volume is 0.222 $mL \cdot g^{-1}$, which may be caused by the gap between particles. However, the isotherm of SiO_x/E@C at $0.4 < P/P_0 < 0.8$ is an approximate horizontal line, indicating that after pitch coating, the number of mesopores of SiO_x/E@C is greatly reduced, and the specific surface area and total pore volume are correspondingly reduced, which are 11.18 $m^2 \cdot g^{-1}$ and 0.058 $mL \cdot g^{-1}$, respectively. This is due to the shrinkage of pitch during high temperature carbonization, and the amorphous carbon generated by carbonization fills the pores of SiO_x/ECP [9]. Due to the addition of CNTs, the staggered CNTs on the surface of SiO_x/E@CPPC make the isotherm of SiO_x/E@CPPC more steep, and a small hysteresis loop appears, meaning that the number of mesopores increases. The specific surface area and the total pore volume also increases to 16.01 $m^2 \cdot g^{-1}$ and 0.096 $mL \cdot g^{-1}$, respectively. The moderate specific surface area and the narrow pore size distribution are beneficial to the transport of electrons and ions, inhibit the side reactions on the surface of the electrode material, and improve the electrochemical performance of SiO_x/E@CPPC [40].

The content of SiO_x in SiO_x/ECP, SiO_x/E@C, and SiO_x/E@CPPC are confirmed by TG tests (Fig. 5c). In the air atmosphere, SiO_x increases by 4.6% after holding at 800 °C for 30 min, which is due to the oxidation of part of SiO_x to SiO_2. The weight loss of SiO_x/ECP begins at about 560 °C, and the weight loss is 1.7% after the test. It is speculated that the content of SiO_x is about 93.7 wt.%, and the content of ECP-600 JD is about 6.3 wt.%. The content of SiO_x is lower than the designed content, which may be owing to the fact that the particle size of ECP-600 JD is too small and easy to agglomerate, giving rise to uneven mixing. SiO_x/E@C begins to lose weight at 450 °C. The content of carbon layer produced by pitch pyrolysis is about 14.8 wt.%, and the content of SiO_x is about 78.9 wt.%. However, SiO_x/E@CPPC begins to lose weight slowly at 200 °C. The total content of PVA, PEI and CNTs is about 4.5 wt.%, and the content of SiO_x is about 74.4 wt.%.

To further verify the composition, chemical valence states of the constituent elements in SiO_x/ECP, SiO_x/E@C, and SiO_x/E@CPPC were analyzed with XPS [41, 42]. Figure 5d exhibits the XPS full spectrum of SiO_x/ECP, SiO_x/E@C, and SiO_x/E@CPPC. All three materials have four peaks at 531.7 eV, 284.2 eV, 152.8 eV, and 101.9 eV, separately corresponding to O 1 s, C 1 s, Si 2 s, and Si 2p. Besides, it can be observed that the percentage of C atoms on the surface of SiO_x/E@C increases from 41.29 to 59.04% after being

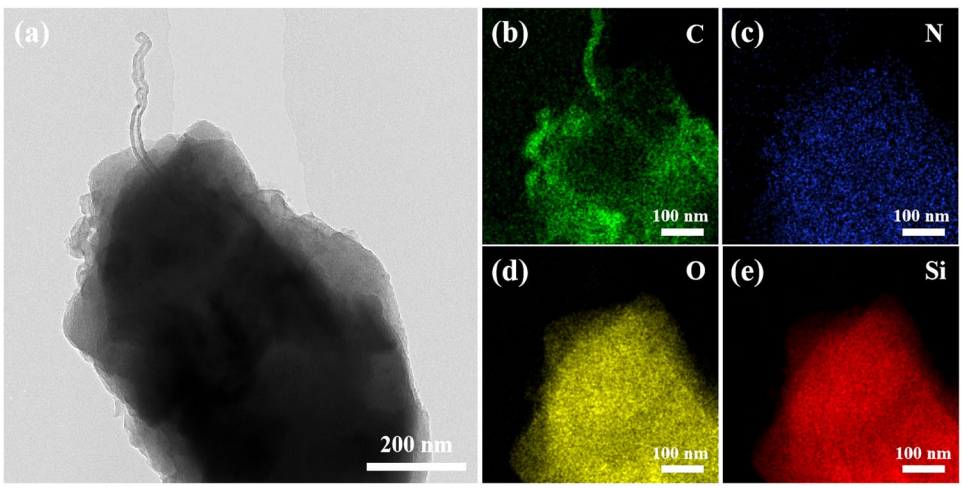

Fig. 4 **a** TEM image of SiO_x/E@CPPC, **b**~**e** EDS element distribution image of SiO_x/E@CPPC

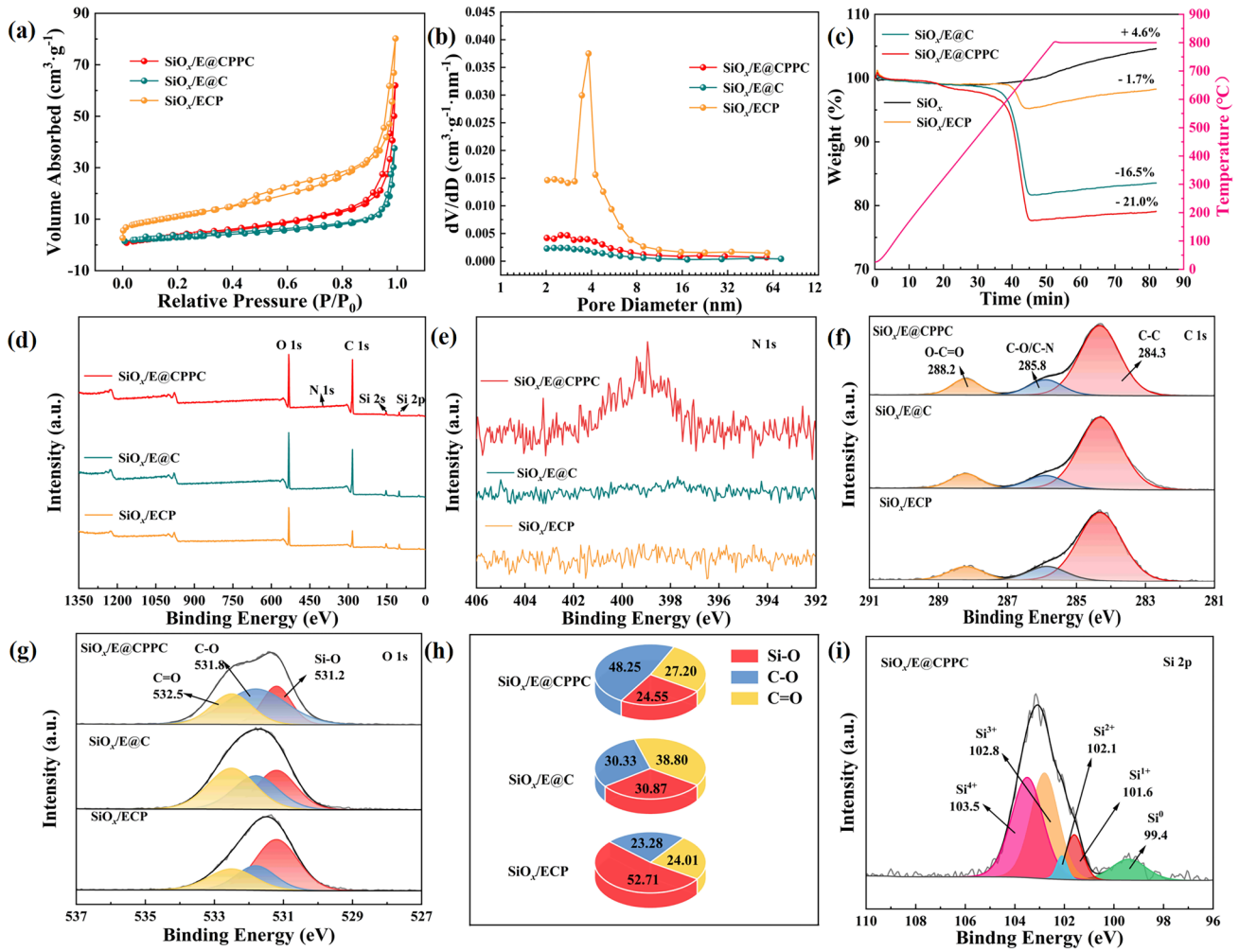

Fig. 5 **a** N_2 adsorption–desorption curves of SiO_x/ECP, SiO_x/E@C and SiO_x/E@CPPC and **b** pore size distribution curve; **c** TG curve, **d** XPS full spectrum, **e** N 1 s spectrum, **f** C 1 s spectrum, **g** O 1 s spectrum, **h** the content of different types of O, and **i** Si 2p spectra of SiO_x/E@CPPC

coated with carbon generated by pitch pyrolysis. After PVA/PEI/CNTs coating, the percentage of C atoms on the surface of SiO_x/E@CPPC increases from 59.04 to 69.82%, the percentage of Si atoms on the surface decreases from 15.32 to 8.30%, and a less obvious N 1 s diffraction peak appears at 399.6 eV. In the fine spectrum of N 1 s of the three materials in Fig. 5e, it can be clearly observed that SiO_x/E@CPPC has a diffraction peak of N 1 s, but it does not appear in the spectrum of SiO_x/ECP and SiO_x/E@C, indicating that PEI exists in SiO_x/E@CPPC. In the C 1 s spectrum of Fig. 5f, it is fitted as C-C (284.3 eV), C-O/C-N (285.8 eV), and O-C=O (288.2 eV) [29, 43, 44]. Compared with SiO_x/ECP, SiO_x/E@C possesses higher C-C content due to carbon coating, and its proportion increases from 75.01 to 79.41%. Because of the addition of PVA and PEI, SiO_x/E@CPPC displays higher C-O/C-N content than SiO_x/E@C, and its proportion increases from 9.49 to 13.74%. For the O 1 s spectrum (Fig. 5g), three fitting peaks at 531.2 eV, 531.8 eV, and 532.5 eV can be observed, which are attributed to Si-O, C-O, and C=O bonds, respectively [45–47]. The specific content distribution map is shown in Fig. 5h. The content of C-O in SiO_x/E@CPPC is 17.92% higher than that of SiO_x/E@C, which is a result of that the addition of PVA brings a large number of C-O bonds. Figure 5i is the Si 2p spectrum of SiO_x/E@CPPC, which can be fitted into five diffraction peaks centered at 99.4 eV, 101.6 eV, 102.1 eV, 102.8 eV, and 103.5 eV, successively belonging to Si^0, Si^+, Si^{2+}, Si^{3+}, and Si^{4+} [7, 48].

3.2 Electrochemical performances of SiO_x/E@CPPC

Figure 6a–c are the CV curves of SiO_x/ECP, SiO_x/E@C, and SiO_x/E@CPPC at 0.1 $mV \cdot s^{-1}$ for 5 cycles, respectively. The CV curves of the three materials are similar, proving that the electrochemical reactions are the same. In the first reduction curves, the unobvious broad peaks at 1.00 V, 1.10 V, and 0.93 V are due to the formation of SEI film and the decomposition of electrolyte additive FEC [49]. The peak

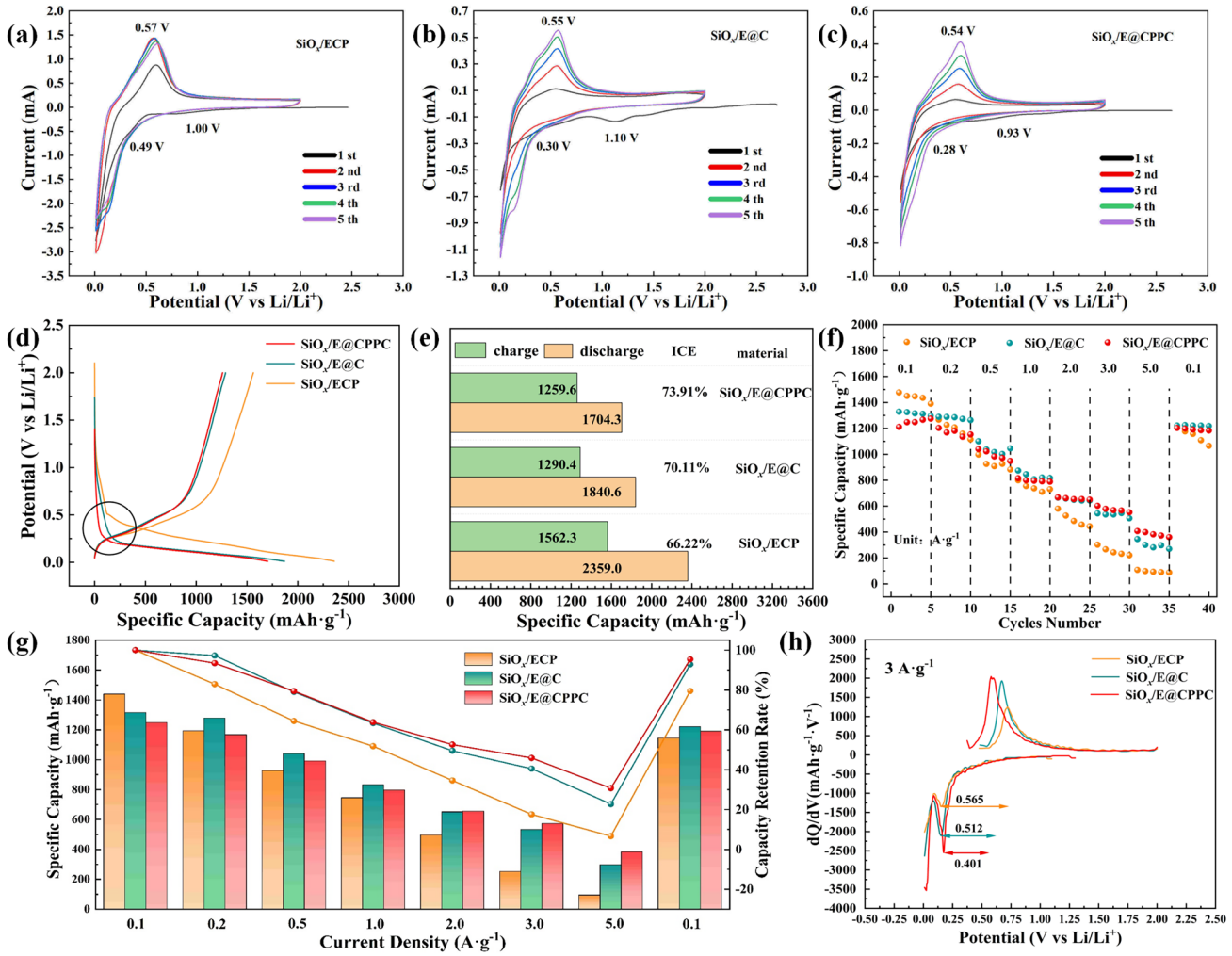

Fig. 6 CV curve of **a** SiO_x/ECP, **b** SiO_x/E@C, **c** SiO_x/E@CPPC; **d** the first charge–discharge curves, **e** the first charge–discharge specific capacity and ICE, **f** rate performance, **g** capacity retention at different current densities, and **h** dQ/dV curve at 3 $A \cdot g^{-1}$ of SiO_x/ECP, SiO_x/E@C, and SiO_x/E@CPPC

disappears in the subsequent cycle, indicating that the SEI film is mainly formed in the first cycle. After that, strong reduction peaks begin to appear at 0.49 V, 0.30 V, and 0.28 V, respectively, corresponding to the reduction of SiO_x to Si, and the formation of Li_2O, lithium silicate, and Li_xSi. The broad peaks of 0.57 V, 0.55 V, and 0.54 V in the first oxidation curve represent the delithiation process of Li_xSi [12]. It is worth noting that in the CV curves of SiO_x/E@C and SiO_x/E@CPPC, the intensity of the reduction peak and the oxidation peak increases with the increase of the number of cycles, manifesting that the electrode material is activated and a good conductive network is formed [50]. In the CV curve of SiO_x/ECP, the intensity of the reduction peak and the oxidation peak in the second cycle is higher than those in the first cycle, and the intensity gradually decreases in the subsequent cycles, suggesting that the structural stability of SiO_x/ECP is poor. After the second cycle of CV scanning, the electrode is gradually destroyed, leading to a decrease in peak intensity [51].

The SiO_x/ECP, SiO_x/E@C, and SiO_x/E@CPPC are assembled into a CR2025 button cell to test the electrochemical performances, and the galvanostatic charge–discharge test is performed at a current density of 0.1 $A \cdot g^{-1}$. The initial charge–discharge curve, charge–discharge specific capacity, and coulombic efficiency are shown in Fig. 6d and e. During the first discharge process of SiO_x/ECP, the discharge voltage decreases rapidly to 1.0 V, and a steep discharge slope appears at 1.0–0.5 V, indicating the formation of SEI film, followed by a long discharge platform at 0.5–0.01 V, indicating the lithium insertion process of the material. In the first charging curve, the charging voltage of SiO_x/ECP gradually increases, showing a large charging slope in the voltage range of 0.01–0.5 V, implying the delithiation process of the material. The initial discharge and charge specific capacities of

SiO_x/ECP are 2359.0 mAh·g^{-1} and 1562.3 mAh·g^{-1}, respectively, and the initial coulombic efficiency is 66.22%. The low coulombic efficiency is mainly due to the formation of SEI film, irreversible Li_2O, and lithium silicate, which consumes a large amount of Li^+. In the first discharge curve of SiO_x/E@C, the formation of SEI film is at 1.0–0.2 V, the discharge platform appears at 0.2–0.01 V, and the charging slope appears at 0.01–0.5 V in the first charging curve. Due to the decrease of SiO_x content, the first charge and discharge specific capacity decreases to 1290.4 mAh·g^{-1} and 1840.6 mAh·g^{-1}, but the ICE increases to 70.11%. This is because the carbon coating effectively reduces the contact area between SiO_x/E@C and the electrolyte, reduces the irreversible lithium loss caused by the formation of SEI film, and reduces the SEI impedance and improves the first coulombic efficiency. The initial charge–discharge specific capacity of SiO_x/E@CPPC is 1259.6 mAh·g^{-1} and 1704.3 mAh·g^{-1}, and the SEI film appears on the steep voltage slope of 1.0–0.25 V. The slope degree corresponds to the degree of side reaction. This means that the irreversible capacity. From Fig. 6e, it can be seen that SiO_x/E@CPPC has the smallest inclination and the highest ICE (73.91%), which is owing to that the flexible and highly conductive interface (PVA/PEI/CNTs) on the surface of SiO_x/E@CPPC can further avoid the direct contact between the internal particles and the electrolyte. At the same time, the content of SiO_x is lower, and the irreversible Li_2O and lithium silicate salt are less.

To explore the electrochemical performances of SiO_x/ECP, SiO_x/E@C, and SiO_x/E@CPPC at high current density, the rate performance of the three materials is tested at the current density range of 0.1–5.0 A·g^{-1} (as shown in Fig. 6f). The charge specific capacity of SiO_x/E@CPPC is 1211.6 mAh·g^{-1} at a current density of 0.1 A·g^{-1}, and the charge specific capacity gradually decreases to 1168.4 mAh·g^{-1}, 993.0 mAh·g^{-1}, 815.5 mAh·g^{-1}, 667.4 mAh·g^{-1}, 602.2 mAh·g^{-1}, and 407.1 mAh·g^{-1} as the current density increases to 0.2 A·g^{-1}, 0.5 A·g^{-1}, 1.0 A·g^{-1}, 2.0 A·g^{-1}, 3.0 A·g^{-1}, and 5.0 A·g^{-1}.

The average specific capacity and the capacity retention rate of five cycles at different current densities are shown in Fig. 6g. The capacity retention rates are 93.47%, 79.48%, 63.86%, 52.59%, 45.91%, and 30.75%, respectively. The calculation method of battery capacity retention rate is the average specific capacity of five cycles at different current densities/the average specific capacity of five cycles at 0.1 A·g^{-1}. When the current density is restored to 0.1 A·g^{-1}, the charge specific capacity is restored to 1203.3 mAh·g^{-1}, which is 95.40% of the first charge capacity. The initial charge specific capacity of SiO_x/E@C is 1328.7 mAh·g^{-1}, and the charge specific capacity at 3.0 A·g^{-1} and 5.0 A·g^{-1} is 543.9 mAh·g^{-1} and 345.3 mAh·g^{-1}, respectively. When the current density is restored to 0.1 A·g^{-1}, the charge specific capacity is restored to 92.85% of the initial charge capacity (1222.2 mAh·g^{-1}). Among the three materials, SiO_x/ECP has the worst rate performance. The charge specific capacity at 3.0 A·g^{-1} and 5.0 A·g^{-1} is only 302.3 mAh·g^{-1} and 108 mAh·g^{-1}, and when the current density is restored to 0.1 A·g^{-1}, the charge specific capacity is only restored to 79.51% of the initial charge capacity. The attenuation of the charging specific capacity of SiO_x/ECP seriously indicates that its structure is unstable. During the lithiation/delithiation process, the SiO_x particles in the electrode undergo serious volume changes, leading to the destruction of the electrode structure. Although the charge specific capacity of SiO_x/E@CPPC at low current density is slightly lower than that of SiO_x/ECP and SiO_x/E@C, when the current density increases to 0.5 A·g^{-1}, the charge specific capacity and capacity retention rate of SiO_x/E@CPPC at subsequent current density are higher than those of SiO_x/ECP and SiO_x/E@C, showing excellent rate performance. When the current density is increased to 5 A·g^{-1}, the charge capacity of SiO_x/E@CPPC anode is 407.1 mAh·g^{-1}, which is higher than the theoretical capacity of commercial graphite anode (372 mAh·g^{-1}).

When charging and discharging at high rates, the internal resistance of the battery increases, resulting in an increase in polarization, so that the charging voltage platform rises and the discharge voltage platform decreases, and the difference between the two platforms increases [52]. The voltage difference of the charge–discharge platform caused by polarization is shown in the dQ/dV curve of Fig. 6h. It can be seen from Fig. 6h that the polarization potential difference between the charge and discharge platforms of SiO_x/E@CPPC is 0.401 V at 3 A·g^{-1}, which are lower than those of SiO_x/ECP and SiO_x/E@C. The SiO_x/E@CPPC exhibits good electrochemical performances at high current densities, indicating that the rigid carbon coating layer and flexible coating layer in SiO_x/E@CPPC ensure the structural stability of the electrode. In the meanwhile, carbon nanotubes provide a fast path for the conduction of electrons and ions.

For studying the excellent rate performance of SiO_x/E@CPPC, the electrochemical kinetics of SiO_x/E@CPPC is studied by measuring the CV curves at 0.1–1.0 mV·s^{-1} (as shown in Fig. 7a–d). The total capacity of the battery can be divided into three parts: (1) battery contributions: the redox reactions are accompanied by the lithiation/delithiation behaviors; (2) pseudo-capacitive contributions: the Faraday capacitance contribution is dominated by surface atomic charge transfer; (3) double-layer capacitance contribution: the Faraday and double-layer capacitive contributions are attributed to capacitive contributions [53]. At present, it is generally believed that the peak current (i_p) and the scanning rate (v) follow a power function relationship in the CV test [54, 55]:

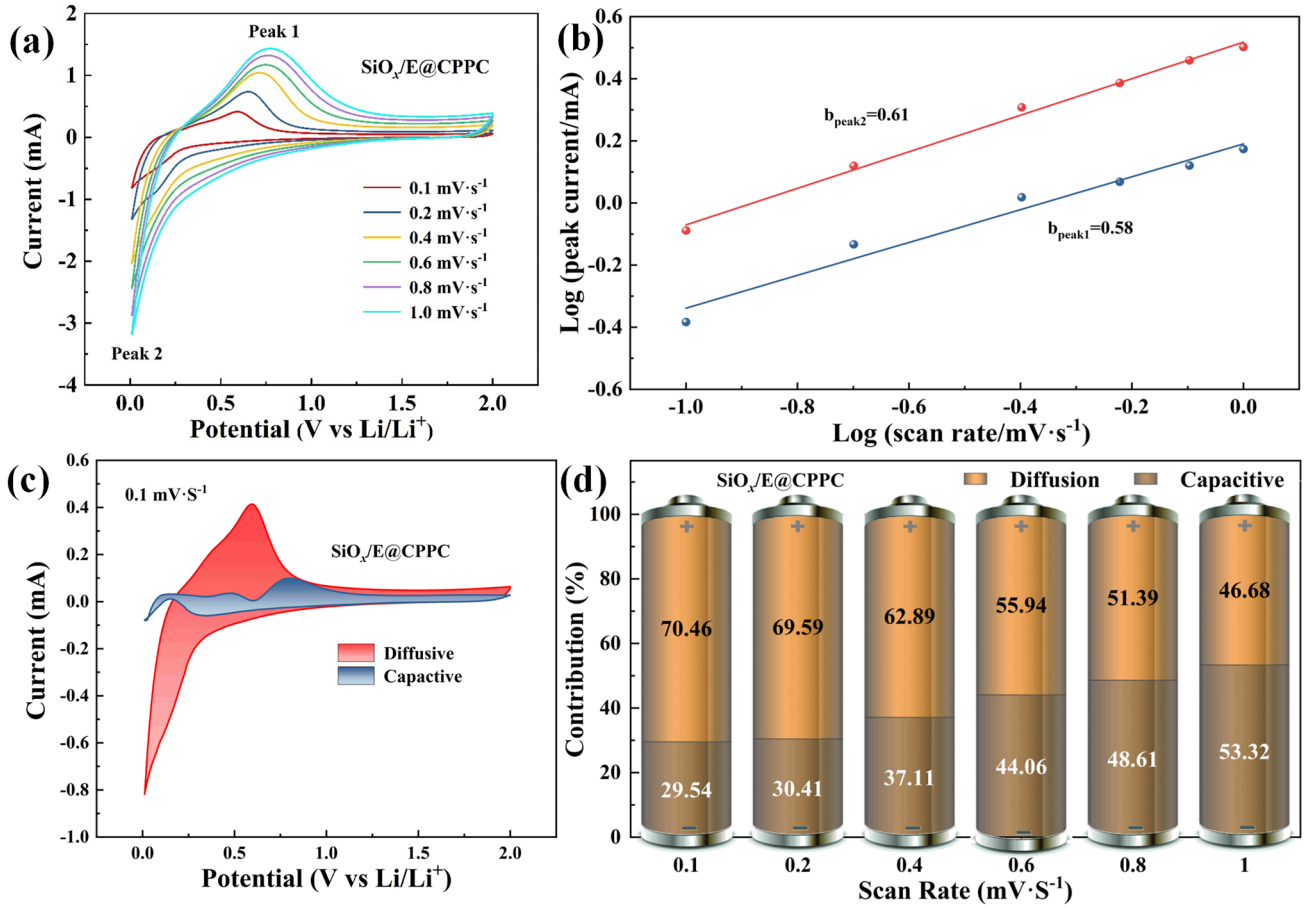

Fig. 7 **a** CV curves of SiO$_x$/E@CPPC at 0.1–1.0 mV·s^{-1}; **b** the line relationship of Log(i, peak current) vs. Log(v, sweep rate) at peak 1, 2 in CV curves; **c** capacitive contribution (blue area) to total lithium storage capacity at a sweep rate of 0.1 mV·s^{-1}; **d** the percentages of capacitive-effect contribution and diffusion-controlled contribution at different sweep rates of 0.1 mV·s^{-1}, 0.2 mV·s^{-1}, 0.4 mV·s^{-1}, 0.6 mV·s^{-1}, 0.8 mV·s^{-1}, and 1.0 mV·s.$^{-1}$

$$i_p = av^b \tag{1}$$

$$lni_p = ln\,a + b\,ln\,v \tag{2}$$

where i_p is the peak current, v is the scan rate, a and b are coefficients. Previous studies have shown that when b is close to 0.5, the capacity is mainly provided by the battery contribution, and when b tends to 1, the capacity is mainly provided by the capacitance contribution. When the b value is between 0.5 and 1, it indicates that the battery is jointly controlled by capacitance and diffusion [53]. The electrochemical behavior is an interface-limited process and more capacitive when the b value is closer to 1, indicating a faster kinetics process [56]. Therefore, we can judge the capacity contribution of the battery by calculating the size of the b value. Using lnv as the abscissa and lnip as the ordinate, the b values of the oxidation peak (Peak1) and the reduction peak (Peak2) of the SiO$_x$/E@CPPC electrode (Fig. 7b) are calculated to be 0.61 and 0.58, respectively, between 0.5 and 1, indicating that most of the capacity is provided by the contribution of the battery, but there is also a capacitance contribution. The capacity of SiO$_x$/E@CPPC contains the capacity of diffusion effect and capacitance effect.

Therefore, at a certain voltage, the total current response i consists of two parts: the reaction current ($k_2v^{0.5}$) contributed by diffusion control and the capacitance-controlled current (k_1v) [57]:

$$i = k_1v + k_2v^{0.5} \tag{3}$$

$$\frac{i}{v^{0.5}} = k_1v^{0.5} + k_2 \tag{4}$$

According to Eq. (4), k_1 and k_2 under different voltages can be calculated by linear fitting of the data at a scanning rate of 0.1 mV·s^{-1}, and then, the capacitance-controlled current k_1v can be calculated. As shown in Fig. 7c, the blue

part of the figure is the capacitance contribution area. By calculating its area and the area of the total CV curve, the capacitance contribution ratio is about 29.54%. This means that the capacitance contribution capacity is 29.54% of the total capacity. In addition, the percentage of capacitance contribution at 0.2, 0.4, 0.6, 0.8, and 1.0 $mV{\cdot}s^{-1}$ is calculated respectively, and the corresponding capacitance contribution is 30.41%, 37.11%, 44.06%, 48.61%, and 53.32%, respectively (as shown in Fig. 7d), and the capacitance contribution generated by capacitance control increased with the increase of scanning rate, indicating that the capacitive behavior played an important role in the total capacity, and the high proportion of capacitive behavior contribution is beneficial to the high rate performance of the battery. Li^+ are difficult to transport into the interior of the active material due to the large impedance at high current. When the material has a pseudo-capacitive contribution behavior, the surface-controlled energy storage behavior can provide additional capacity, which is beneficial to the rate performance of lithium-ion batteries [53]. Therefore, at a higher scan rate, the capacitive behavior on the electrode surface and the redox pseudo-capacitive process occurring on the surface of the active material provide more capacity contribution than the diffusion-controlled slow Li^+ insertion and extraction [57].

The GITT was used to study the change of Li^+ diffusion kinetics during discharge/charge. The Li^+ diffusion coefficients of SiO_x/ECP, SiO_x/E@C, and SiO_x/E@CPPC are analyzed by charging and discharging for 10 min at a current of 0.1 $A{\cdot}g^{-1}$ and then standing for 1 h (as shown in Fig. 8a and c). According to the assumption that Li^+ transport satisfies Fick's second law, the diffusion coefficient D of Li^+ can be calculated by Eq. (5) [58]:

$$D = \frac{4}{\pi\tau}\left[\left(\frac{m_B V_m}{A M_B}\right)\frac{\Delta E_s}{\Delta E_t}\right]^2 \tag{5}$$

In this equation, τ refers to the constant current titration time, A is the area of the electrode, and m_B, M_B, and V_m represent the mass, molar mass, and molar volume of the active material in the electrode, respectively [59]. The $D_{Li}{}^+$ of SiO_x/E@CPPC is the highest during one charge–discharge process, which is in the range of 4.88×10^{-10} to 0.68×10^{-11} $cm^2{\cdot}s^{-1}$, higher than that of SiO_x/E@C ($4.01\times10^{-10}\sim0.47\times10^{-11}$ $cm^2{\cdot}s^{-1}$) and SiO_x/ECP ($3.59\times10^{-10}\sim0.44\times10^{-11}$ $cm^2{\cdot}s^{-1}$). Therefore, we further verify that SiO_x/E@CPPC has faster reaction kinetics than SiO_x/ECP and SiO_x/E@C, which is due to the synergistic effect of highly conductive ECP-600JD, pitch carbon coating and CNTs, which shortens the ion transport path and improves the conductivity of the composite.

EIS tests are performed on SiO_x/ECP, SiO_x/E@C, and SiO_x/E@CPPC samples after rate test. As shown in Fig. 8b, the impedance curves of the three materials are composed

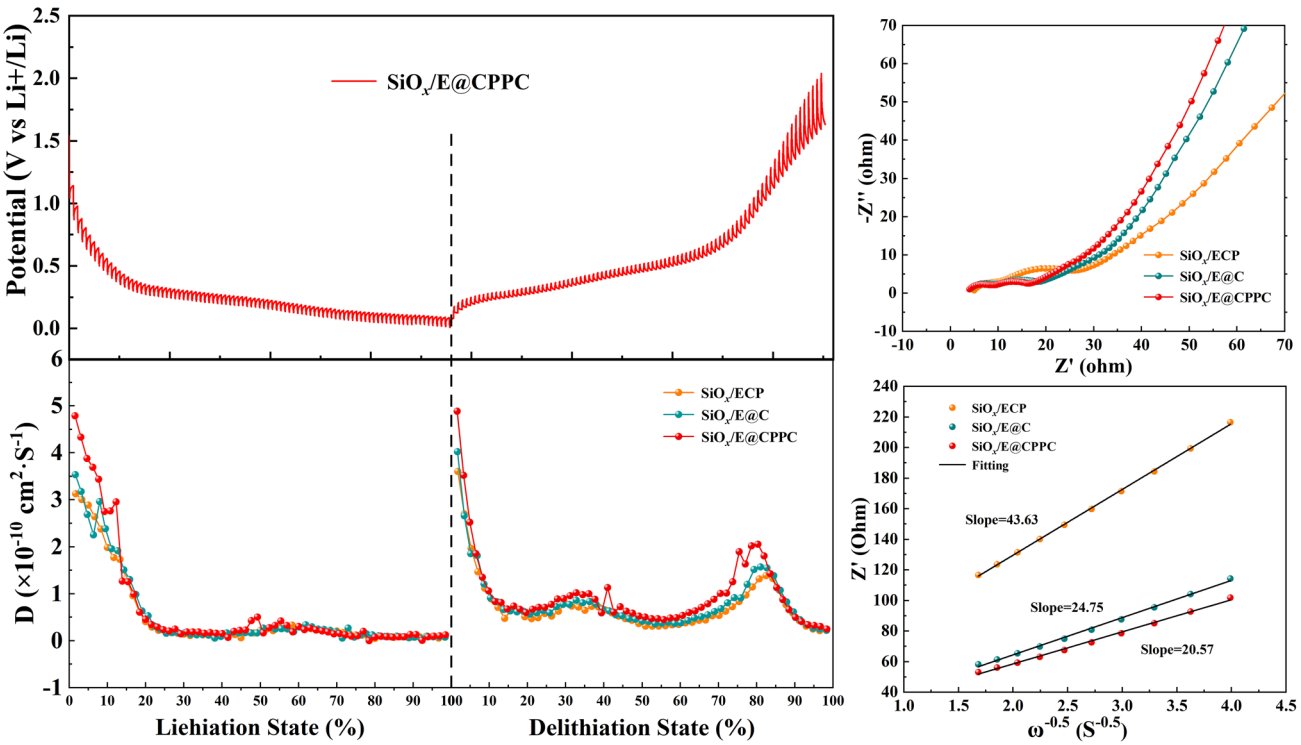

Fig. 8 **a** GITT curves and **c** the corresponding Li^+ diffusion coefficients (D) for the SiO_x/ECP, SiO_x/E@C and SiO_x/E@CPPC during charge–discharge process at 0.1 $A{\cdot}g^{-1}$, **b** EIS curves after cycle and **d** linear fittings in low-frequency region

of two semicircles and an oblique line. The first half circle corresponds to the impedance of the SEI film, the second half circle corresponds to the charge transfer impedance of the electrode–electrolyte interface, and the slash in the low-frequency region is related to the diffusion behavior of Li^+ in the electrode [60]. The equivalent circuit model of the impedance curve of the sample is shown in Fig. 8b, where R_s, R_{SEI}, and R_{ct} represent the electrolyte, SEI film and charge transfer impedance, respectively, and W_o represents the Warburg impedance related to Li^+ diffusion. In general, the smaller the semicircle in the EIS curve, the lower the charge transfer and the impedance of the SEI film. The larger the slope, the faster the diffusion of Li^+ in the electrode. The impedance fitting data of the electrode are shown in Table 1. By comparing the impedance fitting data of SiO_x/ECP and SiO_x/E@C electrodes, it can be found that the resistance of SEI film and charge transfer of SiO_x/E@C is smaller than that of SiO_x/ECP, indicating that the rigid carbon coating in the composite improves the overall conductivity and charge transfer rate of the material. After coating the flexible coating layer with high conductivity on the surface of the particles, the internal resistance is further reduced, especially the R_{ct} value is reduced from 13.13 to 8.42 Ω, which is enough to show that carbon nanotubes can improve the conductivity and interface charge transfer rate of the composite material on the basis of carbon coating, enhancing the electrochemical performance of the material. The Li^+ diffusion coefficients D of SiO_x/ECP, SiO_x/E@C, and SiO_x/E@CPPC are calculated by the formula 6 and 7 [61]. The results are shown in Table 1:

$$D_{Li^+} = \frac{0.5R^2T^2}{A^2F^4C^2\sigma^2} \tag{6}$$

$$Z' = R_s + R_{ct} + \sigma\omega^{-0.5} \tag{7}$$

where R represents the gas constant, T refers to the Kelvin temperature, A refers to the surface area of the electrode, n is the number of electrons transferred during the redox reaction, F is the Faraday constant, and C represents the Li^+ concentration in the electrolyte [61]. σ is the slope of the fitted curve in Fig. 8d, where the real part of the impedance Z' is proportional to $\omega^{-0.5}$. After cycling, the low-frequency region of the SiO_x/E@CPPC electrode has the smallest slope and the highest $D_{Li}{}^+$, which is 1.30×10^{-15} $cm^2{\cdot}s^{-1}$, which is consistent with the excellent rate performance of SiO_x/E@CPPC.

Table 1 Equivalent circuit fitting value, Warburg factor, and Li^+ diffusion coefficient of composites after cycle

Samples	R_{SEI} (Ω)	R_{ct} (Ω)	σ	$D_{Li}{}^+$ ($cm^2{\cdot}s^{-1}$)
SiO_x/ECP	4.97	15.81	43.63	1.02×10^{-15}
SiO_x/E@C	3.18	13.13	24.75	1.04×10^{-15}
SiO_x/E@CPPC	2.88	8.42	20.57	1.30×10^{-15}

In order to explore the cycle stability of SiO_x/ECP, SiO_x/E@C, and SiO_x/E@CPPC electrodes in lithium-ion batteries, after 10 cycles at a low current density (0.1 $A{\cdot}g^{-1}$), the long cycle performance was tested at a current density of 0.5 $A{\cdot}g^{-1}$ for 700 cycles. The results are shown in Fig. 9. The initial charge specific capacity of SiO_x/ECP is 1551.7 $mAh{\cdot}g^{-1}$ at a low current density of 0.1 $A{\cdot}g^{-1}$. After 10 cycles, the current density increases to 0.5 $A{\cdot}g^{-1}$, and the charge specific capacity decreases to 962.0 $mAh{\cdot}g^{-1}$. After 269 cycles, the charge specific capacity decays to less than 100 $mAh{\cdot}g^{-1}$, and only 15.4 $mAh{\cdot}g^{-1}$ (1.6%) remains after 710 cycles. The rapid decay of SiO_x/ECP-specific capacity is mainly due to the destruction of electrode structure caused by the continuous expansion and contraction of SiO_x particles in the composite. After coating SiO_x/ECP with pitch as rigid carbon coating, the rigid carbon coating inhibits the volume change of particles. The cycle stability of SiO_x/E@C is significantly improved compared with SiO_x/ECP. After 710 cycles, the specific capacity maintains at about 527.8 $mAh{\cdot}g^{-1}$, and the capacity retention rate increases to 47.86%. The charge specific capacity of SiO_x/E@CPPC is 1005.5 $mAh{\cdot}g^{-1}$ at a current density of 0.5 $A{\cdot}g^{-1}$. The specific capacity is 704.0 $mAh{\cdot}g^{-1}$ after 500 cycles and 645.8 $mAh{\cdot}g^{-1}$ after 700 cycles. The capacity retention rate is 64.23%. In contrast, SiO_x/E@CPPC has the best cycling performance, which is due to the flexible and highly conductive PVA/PEI/CNTs coating layer further maintaining the structural integrity of the micron size. The CE of SiO_x/E@CPPC reaches 99% after the 9th cycle (Fig. 9b). The average CE of the first 10 cycles is 95.79%, which is higher than that of SiO_x/ECP (93.89%) and SiO_x/E@C (95.16%). The low coulomb efficiency will consume limited Li^+ in practical applications, resulting in serious capacity decay.

Figure 9c_1, d_1, and e_1 show the SEM photos of SiO_x/ECP, SiO_x/E@C, and SiO_x/E@CPPC electrodes before cycling, respectively. The photos show that the morphology of the electrodes prepared by the three materials before cycling is not much different. Figure 9c_2, d_2, and e_2 exhibit the SEM images of the three electrodes after 100 cycles at 0.5 $A{\cdot}g^{-1}$. As shown in Fig. 9c_2, after 100 cycles, a large number of cracks appear on the surface of the SiO_x/ECP electrode, indicating that the pulverization of the active particles is very serious, which causes the detachment between the active material and the current collector, resulting in a large loss and failure of the battery capacity. There are still many cracks on the electrode surface after the cycle of rigid carbon-coated SiO_x/E@C (Fig. 9d_2), but there are many fewer cracks on the surface of SiO_x/E@C than SiO_x/ECP electrode. In contrast, no obvious cracks are observed on the electrode after SiO_x/E@CPPC cycling,

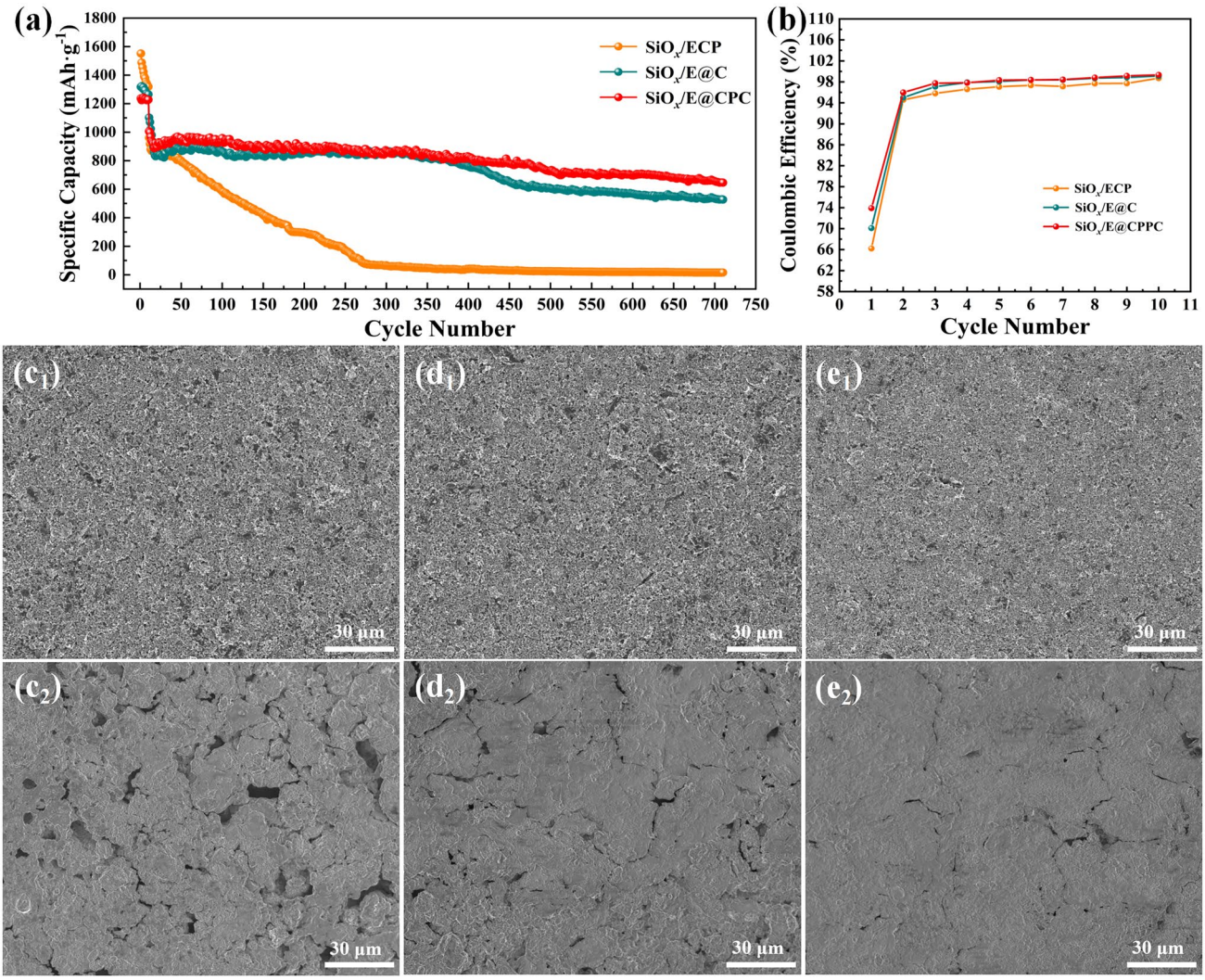

Fig. 9 **a** The cycle performance of SiO_x/ECP, SiO_x//E@C and SiO_x/E@CPPC at 0.5 $A{\cdot}g^{-1}$, **b** the CE of 10 cycles at 0.1 $A{\cdot}g^{-1}$, ($\mathbf{c_1}$) SEM images of SiO_x/ECP electrode before cycling, ($\mathbf{d_1}$) SiO_x/E@C electrode, ($\mathbf{e_1}$) SiO_x/E@CPPC electrode after 100 cycles at 0.5 $A{\cdot}g^{-1}$, ($\mathbf{c_2}$) SEM images of SiO_x/ECP electrode, ($\mathbf{d_2}$) SiO_x/E@C electrode, ($\mathbf{e_2}$) SiO_x/E@CPPC electrode

indicating that the electrode structure maintained good integrity (Fig. 9e_2).

Figure 10 exhibits the structural evolution of SiO_x/ECP, SiO_x/E@C, and SiO_x/E@CPPC electrodes during cycling. As shown in Fig. 10a, SiO_x/ECP is not protected by a carbon coating and is directly exposed to the electrolyte. During the cycle, the huge volume change of SiO_x will lead to the cracking and crushing of particles, so that SiO_x/ECP is separated from the current collector, resulting in rapid capacity decay. During the early cycle of SiO_x/E@C, due to the protection of rigid pitch pyrolytic carbon coating, the damage of particles is not serious. However, after long-term cycle, the rigid carbon coating is not enough to support the long-term volume change of SiO_x/E@C, which still causes some particles to be crushed (Fig. 10b). The SiO_x/E@CPPC particles pass through the rigid carbon coating on the surface and the flexible PVA/PEI/CNTs interface, avoiding the direct exposure of the particles to the electrolyte. The PVA/PEI/CNTs interface, as a conductive enhancer and structural stabilizer, can further improve the bonding strength between the active materials through the mechanical flexibility of PVA and the cross-linking of PVA and the binder PAA during the long-term cycling process, preventing the particles from separating from the current collector. At the same time, the carbon nanotubes wound on the interface can maintain electrical contact with the rigid carbon coating of SiO_x/E@CPPC particles. Ensure good electronic conductivity.

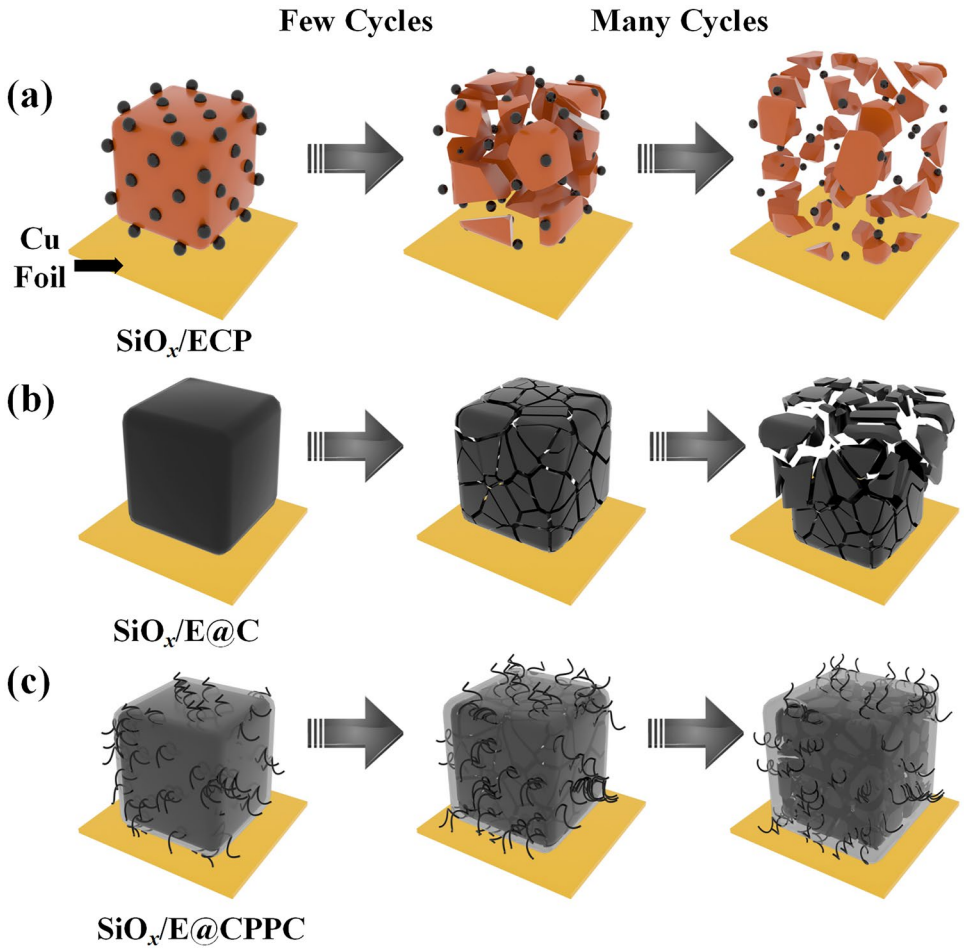

Fig. 10 A schematic diagram of the structural evolution of **a** SiO_x/ECP, **b** SiO_x/E@C, and **c** SiO_x/E@CPPC during the cycling process

4 Conclusions

The conductivity of SiO_x was improved by adding ECP-600JD with excellent conductivity, and then, the rigid carbon coating was prepared by pitch. Finally, a flexible interface with dynamic and stable evolution was established on the surface of the particles to improve the structural stability and rate performance of SiO_x. The flexible coating layer is composed of PVA, PEI, and CNTs, which can maintain the structural integrity of SiO_x particles when the volume changes and aggregate the broken particles when crushing occurs. Moreover, carbon nanotubes help to maintain close contact between particles, thus ensuring the excellent conductivity of SiO_x/E@CPPC particles. Due to the rigid and flexible double-layer interface, the prepared micron-sized SiO_x/E@CPPC particles exhibit high reversible capacity (1211.6 $mAh{\cdot}g^{-1}$ at 0.1 $A{\cdot}g^{-1}$), good rate performance (407.1 $mAh{\cdot}g^{-1}$ at 5 $A{\cdot}g^{-1}$), and excellent cycle stability (645.8 $mAh{\cdot}g^{-1}$ after 700 cycles at 0.5 $A{\cdot}g^{-1}$) in half-cells. The structure design of rigid-flexible double-layer coated micron-sized SiO_x/E@CPPC shows great potential in the practical application of silicon-based anodes.

Supplementary Information The online version contains supplementary material available at https://doi.org/10.1007/s42114-023-00715-3.

Acknowledgements We would like to thank Menghan Sun from Shiyanjia Lab (www.shiyanjia.com) for the TEM analyses.

Author contribution Haidong Xie: data curation, writing-original draft; Yuqing Qu: data curation; Hui Tian: writing—review and editing; Jingying Jiang: methodology; Hui Lu: methodology, review and editing, project administration; Shaolin Yang: writing—review and editing, project administration; Yong Ma: conceptualization, supervision, project administration, writing—review and editing; Chunping Hou: supervision, project administration, writing—review and editing.

Funding This work is financially supported by the National Natural Science Foundation of China (22269001), the Key Research Project of Ningxia Hui Autonomous Region (2021BDE92037), the Key Research and Development Program of Yinchuan (2022XQZD010), and Yinchuan R&D innovation team of advanced energy storage materials and devices (2022CXTD05).

Declarations

Conflict of interest The authors declare no competing interests.

References

1. Liu Z, Yu Q, Zhao Y, He R, Xu M, Feng S, Li S, Zhou L, Mai L (2019) Silicon oxides: a promising family of anode materials for lithium-ion batteries. Chem Soc Rev 48(1):285–309. https://doi.org/10.1039/C8CS00441B
2. Zhou X, Qi Z, Liu Q, Tian J, Liu M, Dong K, Lei Z (2021) Research progress of silicon suboxide-based anodes for lithium-ion batteries. Front Mater. https://doi.org/10.3389/fmats.2020.628233
3. Jiao M, Wang Y, Ye C, Wang C, Zhang W, Liang C (2020) High-capacity SiO_x ($0 \le x \le 2$) as promising anode materials for next-generation lithium-ion batteries. J Alloy Compd 842:155774. https://doi.org/10.1016/j.jallcom.2020.155774
4. Chen T, Wu J, Zhang Q, Su X (2017) Recent advancement of SiO_x based anodes for lithium-ion batteries. J Power Sources 363:126–144. https://doi.org/10.1016/j.jpowsour.2017.07.073
5. Lin Z, Liu T, Ai X, Liang C (2018) Aligning academia and industry for unified battery performance metrics. Nat Commun 9(1):5262. https://doi.org/10.1038/s41467-018-07599-8
6. Wang D, Wang R, Huang K, Lei M, Tang H (2022) Si-P-Ti stabilized Si-P/$Ti_3C_2T_x$ nanohybrids for enhanced lithium-ion storage. Adv Compos Hybrid Ma 5(2):1362–1375. https://doi.org/10.1007/s42114-022-00494-3
7. Lv P, Zhao H, Li Z, Gao C, Zhang Y (2019) Citrate-nitrate gel combustion synthesis of micro/nanostructured SiO_x/C composite as high-performance lithium-ion battery anode. Solid State Ionics 340:115024. https://doi.org/10.1016/j.ssi.2019.115024
8. Liu Q, Hu X, Liu Y, Wen Z (2020) One-step low-temperature molten salt synthesis of two-dimensional Si@SiO_x@C hybrids for high-performance lithium-ion batteries. Appl Mater Inter 12(50):55844–55855. https://doi.org/10.1021/acsami.0c15882
9. Xu Q, Sun J-K, Yin Y-X, Guo Y-G (2018) Facile synthesis of blocky SiO_x/C with graphite-like structure for high-performance lithium-ion battery anodes. Adv Funct Mater 28(8):1705235. https://doi.org/10.1002/adfm.201705235
10. Han M, Yu J (2019) Subnanoscopically and homogeneously dispersed SiO_x/C composite spheres for high-performance lithium ion battery anodes. J Power Sources 414:435–443. https://doi.org/10.1016/j.jpowsour.2019.01.030
11. Yang M, Jin L, He M, Yi Z, Duan T, Yao W (2021) SiO_x@C composites obtained by facile synthesis as anodes for lithium- and potassium-ion batteries with excellent electrochemical performance. Appl Surf Sci 542:148712. https://doi.org/10.1016/j.apsusc.2020.148712
12. Xie H, Hou C, Yue Z, Zhai L, Sun H, Lu H, Wu J, Yang S, Ma Y (2023) Facile synthesis of C, N, P co-doped SiO_x as anode material for lithium-ion batteries with excellent rate performance. J Energy Storage 64:107147. https://doi.org/10.1016/j.est.2023.107147
13. Guo C, Xie Y, Pan K, Li L (2020) MOF-derived hollow SiO_x nanoparticles wrapped in 3D porous nitrogen-doped graphene aerogel and their superior performance as the anode for lithium-ion batteries. Nanoscale 12(24):13017–13027. https://doi.org/10.1039/D0NR02453H
14. He D, Li P, Wang W, Wan Q, Zhang J, Xi K, Ma X, Liu Z, Zhang L, Qu X (2020) Collaborative design of hollow nanocubes, in situ cross-linked binder, and amorphous Void@SiO_x@C as a three-pronged strategy for ultrastable lithium storage. Small 16(5):1905736. https://doi.org/10.1002/smll.201905736
15. Park E, Kim J, Chung DJ, Park M-S, Kim H, Kim JH (2016) Si/SiO_x-conductive polymer core-shell nanospheres with an improved conducting path preservation for lithium-ion battery. Chemsuschem 9(19):2754–2758. https://doi.org/10.1002/cssc.201600798
16. Li G, Huang L-B, Yan M-Y, Li J-Y, Jiang K-C, Yin Y-X, Xin S, Xu Q, Guo Y-G (2020) An integral interface with dynamically stable evolution on micron-sized SiO_x particle anode. Nano Energy 74:104890. https://doi.org/10.1016/j.nanoen.2020.104890
17. Kang T, Ma Z, Zuo X, Xiao X, Nan J (2019) Preparation of flexible self-supporting 3D SiO_x-based membrane anodes with stabilized electrochemical performances for lithium-ion batteries. Energ Technol 7(3):1800635. https://doi.org/10.1002/ente.201800635
18. Li Y, Li S, Sun J (2021) Degradable poly(vinyl alcohol)-based supramolecular plastics with high mechanical strength in a watery environment. Adv Mater 33(13):2007371. https://doi.org/10.1002/adma.202007371
19. Park C-M, Choi W, Hwa Y, Kim J-H, Jeong G, Sohn H-J (2010) Characterizations and electrochemical behaviors of disproportionated SiO and its composite for rechargeable Li-ion batteries. J Mater Chem 20(23):4854–4860. https://doi.org/10.1039/B923926J
20. Ma X, Li L, Chen R, Wang C, Li H, Li H (2018) Highly nitrogen-doped porous carbon derived from zeolitic imidazolate framework-8 for CO_2 capture. Chem-Asian J 13(16):2069–2076. https://doi.org/10.1002/asia.201800548
21. Ruan J, Chang Z, Rong H, Alomar T S, Zhu D, AlMasoud N, Liao Y, Zhao R, Zhao X, Li Y, Xu B B, Guo Z, El-Bahy Z M, Li H, Zhang X, Ge S (2023) High-conductivity nickel shells encapsulated wood-derived porous carbon for improved electromagnetic interference shielding. Carbon 213:118208. https://doi.org/10.1016/j.carbon.2023.118208
22. Xia M, Li Y, Zhou Z, Wu Y, Zhou N, Zhang H, Xiong X (2019) Improving the electrochemical properties of SiO@C anode for high-energy lithium ion battery by adding graphite through fluidization thermal chemical vapor deposition method. Ceram Int 45(2):1950–1959. https://doi.org/10.1016/j.ceramint.2018.10.088
23. Wu W, Kang Y, Wang M, Xu D, Wang J, Cao Y, Wang C, Deng Y (2020) An ultrahigh-areal-capacity SiO_x negative electrode for lithium ion batteries. J Power Sources 464:228244. https://doi.org/10.1016/j.jpowsour.2020.228244
24. Wang R, Wang J, Chen S, Bao W, Li D, Zhang X, Liu Q, Song T, Su Y, Tan G (2021) In situ construction of high-performing compact Si–SiO_x–CN_x composites from polyaminosiloxane for Li-ion batteries. ACS Appl Mater Inter 13(4):5008–5016. https://doi.org/10.1021/acsami.0c18647
25. Zhang L, Zhang L, Zhang J, Hao W, Zheng H (2015) Robust polymeric coating enables the stable operation of silicon micro-plate anodes recovered from photovoltaic industry waste for high-performance Li-ion batteries. J Mater Chem A 3(30):15432–15443. https://doi.org/10.1039/C5TA03750F
26. Yao Y, Xu X, Zhao H, Tong Y, Li Y (2022) Multilayer Si@SiO_x@void@C anode materials synthesized via simultaneously carbonization and redox for Li-ion batteries. Ceram Int 48(9):12217–12227. https://doi.org/10.1016/j.ceramint.2022.01.082
27. Wu Z-H, Yang J-Y, Yu B, Shi B-M, Zhao C-R, Yu Z-L (2019) Self-healing alginate–carboxymethyl chitosan porous scaffold as an effective binder for silicon anodes in lithium-ion batteries. Rare Met 38(9):832–839. https://doi.org/10.1007/s12598-016-0753-0
28. Li T, Wei H, Zhang Y, Wan T, Cui D, Zhao S, Zhang T, Ji Y, Algadi H, Guo Z, Chu L, Cheng B (2023) Sodium alginate reinforced polyacrylamide/xanthan gum double network ionic hydrogels for stress sensing and self-powered wearable device applications. Carbohyd Polym 309:120678. https://doi.org/10.1016/j.carbpol.2023.120678
29. Xu H, Wang Y, Chen R, Bai Y, Li T, Jin H, Wang J, Xia H (2020) A green-synthetic spiderweb-like Si@Graphene-oxide anode material with multifunctional citric acid binder for high energy-density Li-ion batteries. Carbon 157:330–339. https://doi.org/10.1016/j.carbon.2019.10.046

30. Wang X, Zhang Y, Shi Y, Zeng X, Tang R, Wei L (2019) Conducting polyaniline/poly (acrylic acid)/phytic acid multifunctional binders for Si anodes in lithium ion batteries. Ionics 25(11):5323–5331. https://doi.org/10.1007/s11581-019-03122-1
31. Zhang Z, Liu M, Ibrahim MM, Wu H, Wu Y, Li Y, Mersal GAM, El Azab IH, El-Bahy SM, Huang M, Jiang Y, Liang G, Xie P, Liu C (2022) Flexible polystyrene/graphene composites with epsilon-near-zero properties. Adv Compos Hybrid Ma 5(2):1054–1066. https://doi.org/10.1007/s42114-022-00486-3
32. Liu M, Wu H, Wu Y, Xie P, Pashameah RA, Abo-Dief HM, El-Bahy SM, Wei Y, Li G, Li W, Liang G, Liu C, Sun K, Fan R (2022) The weakly negative permittivity with low-frequency-dispersion behavior in percolative carbon nanotubes/epoxy nanocomposites at radio-frequency range. Adv Compos Hybrid Ma 5(3):2021–2030. https://doi.org/10.1007/s42114-022-00541-z
33. Meng X, Li Y, AlMasoud N, Wang W, Alomar T S, Li J, Ye X, Algadi H, Seok I, Li H, Xu B B, Lu N, El-Bahy Z M, Guo Z (2023) Compatibilizing and toughening blends of recycled acrylonitrile-butadiene-styrene/recycled high impact polystyrene blends via styrene-butadiene-glycidyl methacrylate terpolymer. Polymer 272:125856. https://doi.org/10.1016/j.polymer.2023.125856
34. Gao F, Liu Y, Jiao C, El-Bahy SM, Shao Q, El-Bahy ZM, Li H, Wasnik P, Algadi H, Xu BB, Wang N, Yuan Y, Guo Z (2023) Fluorine-phosphate copolymerization waterborne acrylic resin coating with enhanced anticorrosive performance. J Polym Sci. https://doi.org/10.1002/pol.20230108
35. Yang S, Shi C, Qu K, Sun Z, Li H, Xu B, Huang Z, Guo Z (2023) Electrostatic self-assembly cellulose nanofibers/MXene/nickel chains for highly stable and efficient seawater evaporation and purification. Carbon Lett. https://doi.org/10.1007/s42823-023-00540-0
36. Song J, Zhou M, Yi R, Xu T, Gordin ML, Tang D, Yu Z, Regula M, Wang D (2014) Interpenetrated gel polymer binder for high-performance silicon anodes in lithium-ion batteries. Adv Funct Mater 24(37):5904–5910. https://doi.org/10.1002/adfm.201401269
37. Xie P, Shi Z, Feng M, Sun K, Liu Y, Yan K, Liu C, Moussa TAA, Huang M, Meng S, Liang G, Hou H, Fan R, Guo Z (2022) Recent advances in radio-frequency negative dielectric metamaterials by designing heterogeneous composites. Adv Compos Hybrid Ma 5(2):679–695. https://doi.org/10.1007/s42114-022-00479-2
38. Yuan G, Wan T, BaQais A, Mu Y, Cui D, Amin M A, Li X, Xu B B, Zhu X, Algadi H, Li H, Wasnik P, Lu N, Guo Z, Wei H, Cheng B (2023) Boron and fluorine Co-doped laser-induced graphene towards high-performance micro-supercapacitors. Carbon 212:118101. https://doi.org/10.1016/j.carbon.2023.118101
39. Wang C, Liu X, Yang T, Sridhar D, Algadi H, Bin Xu B, El-Bahy Z M, Li H, Ma Y, Li T, Guo Z (2023) An overview of metal-organic frameworks and their magnetic composites for the removal of pollutants. Sep Purif Technol 320:124144. https://doi.org/10.1016/j.seppur.2023.124144
40. Zheng Y, Kong X, Usman I, Xie X, Liang S, Cao G, Pan A (2020) Rational design of the pea-pod structure of SiO_x/C nanofibers as a high-performance anode for lithium ion batteries. Inorg Chem Front 7(8):1762–1769. https://doi.org/10.1039/D0QI00069H
41. Fan G, Wang Z, Sun K, Liu Y, Fan R (2021) Doped ceramics of indium oxides for negative permittivity materials in MHz-kHz frequency regions. J Mater Sci Technol 61:125–131. https://doi.org/10.1016/j.jmst.2020.06.013
42. Moulder JF, Chastain J, King RC (1963) Handbook of X-ray photoelectron spectroscopy: a reference book of standard spectra for identification and interpretation of XPS data. Chem Phys Lett 99:7–10
43. Ge J, Tang Q, Shen H, Zhou F, Zhou H, Yang W, Hong J, Xu B, Saddique J (2021) Controllable preparation of disproportionated SiO_x/C sheets with 3D network as high-performance anode materials of lithium ion battery. Appl Surf Sci 552:149446. https://doi.org/10.1016/j.apsusc.2021.149446
44. Zhang Y, Hu G, Yu Q, Liu Z, Yu C, Wu L, Zhou L, Mai L (2020) Polydopamine sacrificial layer mediated SiO_x/C@C yolk@shell structure for durable lithium storage. Mater Chem Front 4(6):1656–1663. https://doi.org/10.1039/D0QM00120A
45. Guo L, He H, Ren Y, Wang C, Li M (2018) Core-shell SiO@F-doped C composites with interspaces and voids as anodes for high-performance lithium-ion batteries. Chem Eng J 335:32–40. https://doi.org/10.1016/j.cej.2017.10.145
46. Wu J, He X, Li G, Deng J, Chen L, Xue W, Li D (2019) Rapid construction of TiO_2/SiO_2 composite film on Ti foil as lithium-ion battery anode by plasma discharge in solution. Appl Phys Lett 114(4):043903. https://doi.org/10.1063/1.5083686
47. Gong Q, Wang H, Song W, Sun B, Cao P, Gu S, Sun X, Zhou G (2021) Tunable synthesis of hierarchical yolk/double-shelled SiO_x@TiO_2@C nanospheres for high-performance lithium-ion batteries. Chem Eng J 27(8):2654–2661. https://doi.org/10.1002/chem.202003246
48. Li T, Zou YJ, Yin H, Huang YL, Xi C, Kang H, Li C, Zhang J, Lv C, Fan M, Chen Z (2019) Hollow silicon oxide sphere coated with cuprous oxide and polyaniline as an anode for high-performance lithium-ion batteries. NANO 14(03):1950031. https://doi.org/10.1142/S1793292019500310
49. Li M, Yu Y, Li J, Chen B, Konarov A, Chen P (2015) Fabrication of graphene nanoplatelets-supported SiO_x-disordered carbon composite and its application in lithium-ion batteries. J Power Sources 293:976–982. https://doi.org/10.1016/j.jpowsour.2015.06.019
50. Peng M, Qiu Y, Zhang M, Xu Y, Yi L, Liang K (2020) Improved electrochemical performance of SiO-based anode by N, P binary doped carbon coating. Appl Surf Sci 507:145060. https://doi.org/10.1016/j.apsusc.2019.145060
51. Ha J, Park H, Kim M, Kim Y-T, Choi J (2022) Liquefied-natural-gas-derived vertical carbon layer deposited on SiO as cost-effective anode for Li-ion batteries. J Electrochem Soc 169(2):020528. https://doi.org/10.1149/1945-7111/ac4bf1
52. Qi C, Li S, Yang Z, Xiao Z, Zhao L, Yang F, Ning G, Ma X, Wang C, Xu J, Gao J (2022) Suitable thickness of carbon coating layers for silicon anode. Carbon 186:530–538. https://doi.org/10.1016/j.carbon.2021.10.062
53. Dong X, Zheng X, Deng Y, Wang L, Hong H, Ju Z (2020) SiO2/N-doped graphene aerogel composite anode for lithium-ion batteries. J Mater Sci 55(27):13023–13035. https://doi.org/10.1007/s10853-020-04905-y
54. Yan Z, Sun Z, Li A, Liu H, Guo Z, Qian L (2021) Three-dimensional porous flower-like S-doped Fe_2O_3 for superior lithium storage. Adv Compos Hybrid Ma 4(3):716–724. https://doi.org/10.1007/s42114-021-00301-5
55. Lai C, Guo Y, Zhao H, Song H, Qu X, Huang M, Hong SW, Lee K (2022) High-performance double "ion-buffering reservoirs" of asymmetric supercapacitors enabled by battery-type hierarchical porous sandwich-like Co_3O_4 and 3D graphene aerogels. Adv Compos Hybrid Ma 5(3):2557–2574. https://doi.org/10.1007/s42114-022-00532-0
56. Tian H, Tian H, Yang W, Zhang F, Yang W, Zhang Q, Wang Y, Liu J, Silva SRP, Liu H, Wang G (2021) Stable hollow-structured silicon suboxide-based anodes toward high-performance lithium-ion batteries. Adv Funct Mater 31(25):2101796. https://doi.org/10.1002/adfm.202101796
57. Liao C, Wu S (2019) Pseudocapacitance behavior on Fe_3O_4-pillared SiO_x microsphere wrapped by graphene as high performance anodes for lithium-ion batteries. Chem Eng J 355:805–814. https://doi.org/10.1016/j.cej.2018.08.141
58. Huang J, Chen Q, Chen S, Luo L, Li J, Lin C, Chen Y (2021) Al^{3+}-doped $FeNb_{11}O_{29}$ anode materials with enhanced

lithium-storage performance. Adv Compos Hybrid Ma 4(3):733–742. https://doi.org/10.1007/s42114-021-00291-4
59. Zhang K, Du W, Qian Z, Lin L, Gu X, Yang J, Qian Y (2021) SiO_x embedded in N-doped carbon nanoslices: a scalable synthesis of high-performance anode material for lithium-ion batteries. Carbon 178:202–210. https://doi.org/10.1016/j.carbon.2021.03.011
60. Wang K, Tan Y, Li P, Xue B, Sun J (2019) Facile synthesis of double-layer-constrained micron-sized porous $Si/SiO_2/C$ composites for lithium-ion battery anodes. Acs Appl Mater Inter 11(41):37732–37740. https://doi.org/10.1021/acsami.9b12596
61. Xu B, Shen H, Ge J, Tang Q (2021) Improved cycling performance of $SiO_x/MgO/Mg_2SiO_4/C$ composite anode materials for lithium-ion battery. Appl Surf Sci 546:148814. https://doi.org/10.1016/j.apsusc.2020.148814